Fuselage boundary-layer refraction of fan tones radiated from an installed turbofan aero-engine[a)]

James Gaffney and Alan McAlpine[b)]

Institute of Sound and Vibration Research, University of Southampton, Southampton, SO17 1BJ, UK

Michael J. Kingan

Department of Mechanical Engineering, University of Auckland, Auckland, New Zealand

February 6, 2017

[a)] Part of this work was presented in "Sound radiation of fan tones from an installed turbofan aero-engine: fuselage boundary-layer refraction effects", Proceedings of the 22nd AIAA/CEAS Aeroacoustics conference, Paper no. AIAA-2016-2878, Lyon, France, 30 May–1 June 2016.

[b)] Author to whom correspondence should be addressed. Electronic mail: am@isvr.soton.ac.uk

Abstract

A distributed source model to predict fan tone noise levels of an installed turbofan aero-engine is extended to include the refraction effects caused by the fuselage boundary layer. The model is a simple representation of an installed turbofan, where fan tones are represented in terms of spinning modes radiated from a semi-infinite circular duct, and the aircraft's fuselage is represented by an infinitely long, rigid cylinder. The distributed source is a disc, formed by integrating infinitesimal volume sources located on the intake duct termination. The cylinder is located adjacent to the disc. There is uniform axial flow, aligned with the axis of the cylinder, everywhere except close to the cylinder where there is a constant thickness boundary layer. The aim is to predict the near-field acoustic pressure, and in particular to predict the pressure on the cylindrical fuselage which is relevant to assess cabin noise. Thus no far-field approximations are included in the modelling. The effect of the boundary layer is quantified by calculating the area-averaged mean square pressure over the cylinder's surface with and without the boundary layer included in the prediction model. The sound propagation through the boundary layer is calculated by solving the Pridmore-Brown equation. Results from the theoretical method show that the boundary layer has a significant effect on the predicted sound pressure levels on the cylindrical fuselage, owing to sound radiation of fan tones from an installed turbofan aero-engine.

I. Introduction

Organisations such as the International Civil Aviation Organisation (ICAO) and the American Federal Aviation Administration (FAA) oversee noise certification of civil aircraft, including setting stringent targets for the reduction of noise. To aid meeting these requirements, practical and reliable noise prediction methods are an essential part of the research and development toolkit. This paper presents a new theoretical method to predict the sound radiation of fan tones from an installed turbofan aero-engine, focussing on the prediction of the fuselage sound pressure levels (SPL), and how these levels are affected by refraction effects caused by the fuselage boundary layer.

Noise from aero-engines has a major impact on communities around airports as well as the passengers and crew aboard the aircraft. At take-off and cruise conditions the aero-engines are the dominant source of noise from civil aircraft. A turbofan engine represents a very complex noise source, and as such the noise generation and radiation mechanisms are difficult to model accurately. The complexity is compounded by the presence of the airframe. Consequently, turbofan noise models often predict the sound radiated into free space. However, the radiated noise is affected by the whole aircraft, including the fuselage, wings, high-lift devices, landing gear etc. How the radiated acoustic field is affected by interaction with the airframe is referred to as installation acoustics.

This paper will focus on prediction of the sound pressure levels on an aircraft fuselage. The key aim is to develop a simple installation acoustics method based on a canonical problem: how to predict the pressure field due to a source located near an infinite, rigid cylinder. The basis of the method is a classical problem: acoustic scattering by a cylinder. The analytical solution for the acoustic field due to a point source located adjacent to an infinite cylinder is given in the text by Bowman, Senior and Uslenghi (Chapter 2, §2.5.2, pp. 126–127) [1]. Simplifications in the geometry and the mean flow must be made to use analytical techniques, but these do not necessarily curtail the usefulness of the solutions. In this case, the aircraft's fuselage is represented by the cylinder. Also, except close to the fuselage, the flow is assumed to be uniform and its direction is aligned with the axis of the cylinder.

Of principal interest in this current work is the effect of the fuselage boundary layer. One of the earliest examples of work in this area is by Hanson [2] who studied the problem of a point source over a rigid flat plate with a boundary layer. Subsequently, Hanson and Magliozzi [3] examined the more advanced and realistic problem of an open-rotor source located adjacent to a cylindrical fuselage, and with the inclusion of the fuselage boundary layer. This type of model also has been investigated by Lu [4], who utilized a point source model. Most recently Brouwer [5] studied the effects of a boundary layer on the near side of a cylinder for an open-rotor type source. The model was extended to the far-field where there was a modest effect on the free-field predictions caused by the boundary layer.

Historically, these type of theoretical methods for fuselage installation acoustics have focused on open-rotor noise sources. More recently, the procedure given by Hanson and Magliozzi was followed by McAlpine, Gaffney and Kingan [6] to develop a scattering model for a realistic turbofan source located adjacent to an infinitely long, rigid cylindrical fuselage. A disc source was formulated so that the source distribution was representative of sound radiation for a ducted fan noise source. The source is a disc formed by integrating infinitesimal volume sources located on the duct termination. The source strength (volume velocity) is proportional to the axial component of the particle velocity at the duct termination, following the Kirchhoff approximation. Originally Tyler and Sofrin [7] used this approach to construct a Rayleigh integral in terms of a non-uniform velocity distribution across the duct termination. The particle velocity is given by the well-known 'spinning' mode solution for sound propagation in a cylindrical waveguide. Thus, tones generated by a ducted fan are modelled in terms of spinning modes propagating inside the intake duct. This approach neglects diffraction effects at the duct lip, but Hocter [8] has shown that these are largely insignificant for sound radiation up to approximately 70 degrees relative to the axis of the duct. Accordingly, the scattering model is only valid for sound radiation in the forward arc.

This paper extends recent work published in Ref. [6]. The key advancement is the inclusion of the effect of boundary-layer refraction in the modelling. The cylindrical fuselage is in the near-field of the source. Thus it is not valid to use a far-field approximation of the sound field radiated by the source, à la the far-field solution of the Rayleigh integral for a circular disc source. In Ref. [6] the ducted fan noise source was incorporated into a cylinder scattering model with uniform mean flow everywhere. In this paper, the same method for a ducted fan noise source is extended to include refraction effects caused by a boundary layer of constant thickness on the cylindrical fuselage.

II. Theory

A. Fuselage scattering

The acoustic pressure field owing to a fan tone radiated from an intake duct located adjacent to an infinitely long, rigid cylindrical fuselage was derived in McAlpine, Gaffney and Kingan [6]. A sketch of the problem set-up is shown in Figure 1; also shown is some of the nomenclature used in the solution, and the Cartesian reference frames for the source (x, y, z) and the cylinder $(\bar{x}, \bar{y}, \bar{z})$. The equivalent cylindrical polar coordinate reference frames are (r, ϕ, z) for the source and $(\bar{r}, \bar{\phi}, \bar{z})$ for the cylinder. There is a subsonic uniform mean flow, Mach number M_∞, directed in the negative $\bar{z}$-direction. The total pressure field (sum of the incident and scattered fields) is calculated in the

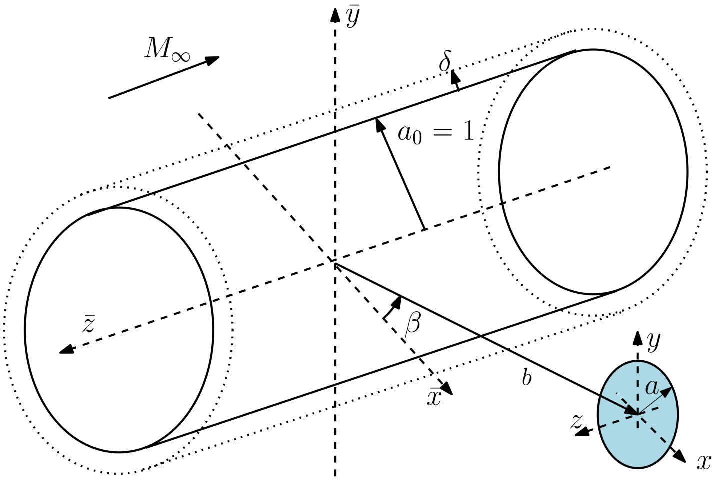

Figure 1: Sketch of the cylindrical fuselage (radius a_0) and the disc source (radius a). The centreline of the cylinder is aligned with the $\bar{z}$-axis. The disc source is located in the plane $\bar{z} = 0$, and the distance between the centre of the disc and the centre of the cylinder is b. Also shown is the edge of the fuselage boundary-layer (thickness δ).

forward arc $\bar{z} > 0$.

From Ref. [6], the time-harmonic total pressure $p_t\left(\bar{r}, \bar{\phi}, \bar{z}, t\right) = \hat{p}_t\left(\bar{r}, \bar{\phi}, \bar{z}\right) \exp\{\mathrm{i}\omega_0 t\}$, is expressed in terms of a Fourier series, and each Fourier harmonic is itself expressed in terms of an inverse Fourier transform. The result from Ref. [6] can be written in non-dimensional form as

$$\hat{p}_t\left(\bar{r}, \bar{\phi}, \bar{z}\right) = \frac{1}{(2\pi)^2} \sum_{n=-\infty}^{\infty} \left\{ \int_{-\infty}^{\infty} \left(\widetilde{p}_{i_n} + \widetilde{p}_{s_n}\right) \mathrm{e}^{-\mathrm{i}k_z \bar{z}} \mathrm{d}k_z \right\} \mathrm{e}^{-\mathrm{i}n\bar{\phi}} , \tag{1}$$

where the incident field

$$\widetilde{p}_{i_n}\left(\bar{r}, k_z\right) = \pi^2 \xi_{lq} P_{lq} (-1)^{l+n} \mathrm{e}^{-\mathrm{i}(l-n)\beta} \left(k_0 + k_z M_\infty\right) \Psi_{lq} \mathrm{H}^{(2)}_{l-n}(\Gamma_0 b) \mathrm{J}_n(\Gamma_0 \bar{r}) , \tag{2}$$

and the scattered field

$$\widetilde{p}_{s_n}\left(\bar{r}, k_z\right) = -\pi^2 \xi_{lq} P_{lq} (-1)^{l+n} \mathrm{e}^{-\mathrm{i}(l-n)\beta} \left(k_0 + k_z M_\infty\right) \Psi_{lq} \frac{\mathrm{H}^{(2)}_{l-n}(\Gamma_0 b) \mathrm{J}'_n(\Gamma_0)}{\mathrm{H}^{(2)\prime}_n(\Gamma_0)} \mathrm{H}^{(2)}_n(\Gamma_0 \bar{r}) , \tag{3}$$

where $\widetilde{\cdot}$ denotes variables which have been Fourier transformed. The Bessel function of the first kind of order ℓ is denoted by J_ℓ, and the Hankel function of the second kind of order ℓ is denoted by $\mathrm{H}^{(2)}_\ell$. The $'$ denotes differentiation with respect to the function's argument. Full details are in McAlpine, Gaffney and Kingan [6].

In Equations (1–3), all the variables have been made non-dimensional by taking the reference length scale equal to the radius of the cylinder, a_0, the reference velocity equal to the speed of sound, c_0, and the reference density equal to the ambient density, ρ_0. Then the pressure is scaled by $\rho_0 c_0^2$.

The fan tone source is modelled by the time-harmonic spinning mode (l, q), where l denotes the azimuthal order and q denotes the radial order. The mode has amplitude P_{lq}, wavenumber k_0 and angular frequency ω_0. The dispersion relationship for the mode is

$$k_{z_{lq}}^2 + \kappa_{lq}^2 = \left(k_0 + k_{z_{lq}} M_\infty\right)^2 , \tag{4}$$

and the mode amplitude coefficient

$$\xi_{lq} = \frac{k_{zlq}}{\left(k_0 + k_{zlq} M_\infty\right)} \, . \tag{5}$$

The term Ψ_{lq} is found by integration over the disc source. This integral can be evaluated exactly. For non-plane-wave excitation, for $r > a$

$$\Psi_{lq} = \begin{cases} \frac{\Gamma_0 a}{\left(\kappa_{lq}^2 - \Gamma_0^2\right)} \mathrm{J}_l(\kappa_{lq} a) \mathrm{J}_l'(\Gamma_0 a) & \text{if } \Gamma_0 \neq \kappa_{lq} \\ \frac{1}{2}\left(a^2 - \frac{l^2}{\kappa_{lq}^2}\right) \mathrm{J}_l^2(\kappa_{lq} a) & \text{if } \Gamma_0 = \kappa_{lq} \end{cases} , \tag{6}$$

and for plane-wave excitation

$$\Psi_{01} = \begin{cases} -\frac{a}{\Gamma_0} \mathrm{J}_0'(\Gamma_0 a) & \text{if } \Gamma_0 \neq 0 \\ \frac{1}{2} a^2 & \text{if } \Gamma_0 = 0 \end{cases} . \tag{7}$$

Similar to Equation (4), the ‘radial’ wavenumber of the radiated field, Γ_0, is given by

$$\Gamma_0^2 = \left(k_0 + k_z M_\infty\right)^2 - {k_z}^2 \, , \tag{8}$$

and equals zero at

$$k_z^- = -\frac{k_0}{1 + M_\infty} \quad \text{and} \quad k_z^+ = \frac{k_0}{1 - M_\infty} \, . \tag{9}$$

From Equations (8) and (9), the wavenumber Γ_0 is defined as

$$\Gamma_0 = -\mathrm{i}\sqrt{1 - M_\infty^2} \sqrt{-\mathrm{i}\left(k_z - k_z^+\right)} \sqrt{\mathrm{i}\left(k_z - k_z^-\right)} \, , \tag{10}$$

on taking the principal value of the square root. In the range $k_z^- < k_z < k_z^+$, the wavenumber Γ_0 is real and positive, and corresponds to wavenumbers which radiate to the far field. Outside of this range, $\Gamma_0 = -\mathrm{i}\gamma_0$ where $\gamma_0 = \sqrt{k_z^2 - (k_0 + k_z M_\infty)^2} > 0$. This wavenumber range corresponds to an evanescent field. Accordingly, the integration of the inverse Fourier transform in Equation (1) is split into three parts as shown in Table 1. Moreover, the definition of Γ_0 given by Equation (10) also

Label	Limits		Γ_0
	lower	higher	
I_1	$-\infty$	k_z^-	$-\mathrm{i}\gamma_0$
I_2	k_z^-	k_z^+	$\sqrt{(k_0 + M_\infty k_z)^2 - k_z^2}$
I_3	k_z^+	∞	$-\mathrm{i}\gamma_0$

Table 1: Breakdown of the inverse Fourier transform integral in Equation (1). The full integral is given by $I_1 + I_2 + I_3$. The value of the wavenumber Γ_0 in each region is specified.

prescribes the appropriate location of the branch cuts from points k_z^- and k_z^+ such that on taking the inverse Fourier transform the radiation conditions will be correct.

Measured relative to the axis of the intake duct (z), as the source Helmholtz number $k_0 a$ increases, the mode and propagation angles also increase. There are several ways that can be used to predict the radiation angle of the principal lobe. One estimate is given by the mode (or phase) angle, which can be calculated directly from the dispersion relationship (4). Rice [9] derived an alternative expression for the radiation angle, viz.

$$\cos\theta = \sqrt{1 - M_\infty^2}\left\{\frac{1 - 1/\zeta^2}{1 - M_\infty^2\,(1 - 1/\zeta^2)}\right\}^{1/2}, \tag{11}$$

where ζ is the cut-off ratio

$$\zeta = \frac{k_0}{k_{zlq}\sqrt{1 - M_\infty^2}}\,. \tag{12}$$

This result is commonly used to predict the principal radiation angle in the presence of flow.

Alternatively the radiation angle can be found numerically by direct computation of the directivity function. For the disc source, the radiated pressure field, expressed in the source coordinates

(r, ϕ, z), is given by

$$\hat{p}_i\left(r, \phi, z\right) \;=\; \frac{\xi_{lq} P_{lq}}{4} \int_{-\infty}^{\infty} \left(k_0 + k_z M_\infty\right) \Psi_{lq} \, \mathrm{H}_l^{(2)}\left(\Gamma_0 r\right) \mathrm{e}^{-\mathrm{i} k_z z} \, \mathrm{d}k_z \, \mathrm{e}^{-\mathrm{i} l \phi} \,, \tag{13}$$

at field points $r > a$. Equation (13) is taken from McAlpine, Gaffney and McAlpine ([6], Eq. (20)).

The location on the cylinder's surface where the SPL is at a maximum can be estimated utilizing the radiation angle of the principal lobe and simple geometry. An example of this is shown in Figure 2. Numerical evaluation of the radiation angle provides the closest estimate to the location of the maximum SPL on the cylinder. This is because the cylinder is located in the near field, whereas the analytic formulas for the mode and propagation angles are valid in the far field.

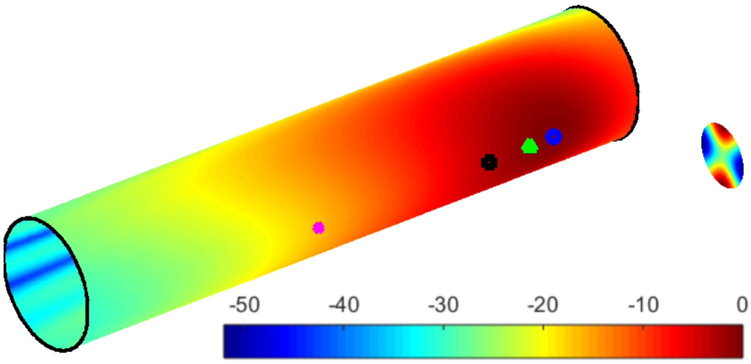

Figure 2: Normalised total SPL on the surface of the cylinder. The location of the maximum value of the SPL is shown by the blue dot. Predictions of this point obtained using (i) mode (phase) angle, (ii) radiation angle (11), or (iii) numerical evaluation of the near-field (in the absence of the cylinder), are also shown. Key: (i) magenta dot; (ii) black dot; (iii) green dot. Other relevant parameters in this example are $(l, q) = (2, 1)$, $k_0 a = 5$, $b = 3$ and $M_\infty = 0.5$.

B. Fuselage scattering including boundary-layer refraction

The technique to include the boundary layer in the method is outlined in this section. A sketch of the cylindrical fuselage, including the constant-thickness boundary layer is shown in Figure 1. The velocity profile M_z is given by

$$M_z = \begin{cases} M(\bar{r}) & 1 < \bar{r} \leq 1 + \delta \\ M_\infty & 1 + \delta < \bar{r} \end{cases} , \qquad (14)$$

where δ is the non-dimensional thickness of the boundary-layer, and $M(\bar{r})$ is the boundary-layer Mach number profile which is assumed to be a smooth, monotonically increasing function. Note that the non-dimensional radius of the fuselage is unity.

Outside the boundary layer, where the source is located, there is uniform flow and the acoustic pressure field is found by solving the convected wave equation. Inside the boundary layer region, the pressure field, p_{bl}, will satisfy the Pridmore-Brown equation.

An inviscid, compressible, isentropic, perfect gas flow is assumed. Additionally, the mean flow is assumed to be axisymmetric and parallel, with constant mean density and sound speed profiles inside the boundary layer. The appropriate field equation for the pressure which captures the refractive effects of the sheared mean flow is given by

$$\frac{\mathrm{D}_0}{\mathrm{D}t}\left(\frac{\mathrm{D}_0^2 p_{bl}}{\mathrm{D}t^2} - \nabla^2 p_{bl}\right) - 2\frac{\mathrm{d}M}{\mathrm{d}\bar{r}}\frac{\partial^2 p_{bl}}{\partial\bar{r}\partial\bar{z}} = 0 \, . \qquad (15)$$

In order to determine the acoustic pressure field everywhere, the solution outside the boundary layer will be matched to the solution inside the boundary layer, whilst ensuring that the appropriate boundary and radiation conditions are satisfied.

On Fourier transforming Equation (15), it reduces to

$$\left[\frac{\mathrm{d}^2}{\mathrm{d}\bar{r}^2} + \left(\frac{1}{\bar{r}} - \frac{2k_z}{k_0 + k_z M}\frac{\mathrm{d}M}{\mathrm{d}\bar{r}}\right)\frac{\mathrm{d}}{\mathrm{d}\bar{r}} + \left(\Gamma_0^2 - \frac{n^2}{\bar{r}^2}\right)\right]\widetilde{p}_{bl_n} = 0 \, , \qquad (16)$$

which is referred to as the Pridmore-Brown equation. A key feature of this equation is that it has a regular singularity at $k_0 + k_z M(\bar{r}_c) = 0$. Where this occurs, referred to as the critical layer, the phase speed equals the local flow velocity. Equation (16) can be solved by numerical integration across the boundary layer. However, special treatment must be given to the solution in the critical layer region.

Following the previous literature [3, 4, 10], a Frobenius solution is used to bridge the singularity at $\bar{r} = \bar{r}_c$. Introducing the critical layer coordinate

$$\varsigma = \bar{r} - \bar{r}_c \, , \tag{17}$$

two independent solutions of the transformed Pridmore-Brown equation (16) in the critical layer are given, up to $\mathrm{O}(\varsigma^3)$, by

$$\widetilde{p}_{bl_{n\,F1}} = \alpha_{F1}\varsigma^3, \tag{18}$$

$$\widetilde{p}_{bl_{n\,F2}} = \alpha_{F2}\left(1 - \frac{1}{2}\left(k_z^2 + \frac{n^2}{\bar{r}^2}\right)\varsigma^2 + \Omega\alpha_{F1}\varsigma^3\ln\varsigma\right) \, , \tag{19}$$

where α_{F1} and α_{F1} are constants, and

$$\Omega = -\frac{1}{3}\left(\frac{M''(\bar{r}_c)}{M'(\bar{r}_c)} - \frac{1}{\bar{r}_c}\right)\left(k_z^2 + \frac{n^2}{\bar{r}_c^2}\right) - \frac{2n^2}{3\bar{r}_c^3} \, . \tag{20}$$

Note that these results are for a general boundary-layer profile; M' and M'' denote the first and second radial derivative of the mean-flow profile respectively. Following the discussion in Hanson and Magliozzi ([3], p. 66), for $\varsigma < 0$, i.e. $\bar{r} < \bar{r}_c$, the branch of the log function in Equation (19) is taken to be $\ln|\varsigma| + \mathrm{i}\pi$.[11] On taking a linear profile this result is found to be in agreement with Refs. [10, 12].

There is no known analytical solution to the Pridmore-Brown equation, therefore a numerical integration routine is utilised. The transformed pressure in the boundary layer is normalised, i.e.

$$\widetilde{p}_{bl_n}\left(\bar{r}, k_z\right) = \widetilde{\alpha}_n(k_z)\widetilde{f}_{bl_n}\left(\bar{r}, k_z\right) \, , \tag{21}$$

where $\widetilde{f}_{bl_n}$ is the normalised pressure, which is scaled by $\widetilde{\alpha}_n(k_z)$. The integration, starting from the surface of the cylinder at $\bar{r} = 1$, is calculated numerically by expressing the Pridmore-Brown equation as two first-order differential equations, viz.

$$\begin{bmatrix} x_2' \\ \\ x_1' \end{bmatrix} = \begin{bmatrix} -\left(\frac{1}{\bar{r}} - \frac{2k_z M'}{k_0 + k_z M}\right) & -\left(\Gamma_0^2 - \frac{n^2}{\bar{r}^2}\right) \\ \\ 1 & 0 \end{bmatrix} \begin{bmatrix} x_2 \\ \\ x_1 \end{bmatrix} , \tag{22}$$

where $x_1 = \widetilde{f}_{bl_n}$ and $x_2 = \mathrm{d}\widetilde{f}_{bl_n}/\mathrm{d}\bar{r} = \widetilde{f}'_{bl_n}$. On the surface of the rigid cylinder, the transformed pressure is set nominally to be $\widetilde{f}_{bl_n}(1, k_z) = 1$, and the derivative $\widetilde{f}'_{bl_n}(1, k_z) = 0$.[13] Accordingly, the boundary conditions on the cylinder are

$$\widetilde{p}_{bl_n}(1, k_z) = \widetilde{\alpha}_n \quad \text{and} \quad \widetilde{p}'_{bl_n}(1, k_z) = 0 \, . \tag{23}$$

The value of $\widetilde{\alpha}_n$ must be proportional to the incoming wave. The pressure and its derivative at the edge of the boundary layer can be used to formulate $\widetilde{\alpha}_n$ in terms of the incident wave amplitude. Applying continuity of pressure and the pressure gradient at the edge of the boundary layer

$$\widetilde{\alpha}_n \widetilde{f}_{bl_n}\big|_{\bar{r}=1+\delta} = \widetilde{\eta}_n \mathrm{J}_n\left(\Gamma_0 \bar{r}\right)\big|_{\bar{r}=1+\delta} + \widetilde{\gamma}_n \mathrm{H}_n^{(2)}\left(\Gamma_0 \bar{r}\right)\big|_{\bar{r}=1+\delta} \, , \tag{24a}$$

$$\widetilde{\alpha}_n \widetilde{f}'_{bl_n}\big|_{\bar{r}=1+\delta} = \widetilde{\eta}_n \Gamma_0 \mathrm{J}'_n\left(\Gamma_0 \bar{r}\right)\big|_{\bar{r}=1+\delta} + \widetilde{\gamma}_n \Gamma_0 \mathrm{H}_n^{(2)\prime}\left(\Gamma_0 \bar{r}\right)\big|_{\bar{r}=1+\delta} \, , \tag{24b}$$

where $\widetilde{\eta}_n(k_z)$ and $\widetilde{\gamma}_n(k_z)$ are amplitude coefficients of the incident and scattered waves respectively. The pressure in the boundary layer is scaled to match the amplitude of the incoming wave, i.e.

$$\widetilde{\alpha}_n(k_z) = -\frac{2\mathrm{i}}{\pi[1+\delta]} \frac{\widetilde{\eta}_n}{\left(\widetilde{f}_{bl_n}\Big|_{1+\delta} \Gamma_0 \mathrm{H}_n^{(2)\prime}\left(\Gamma_0[1+\delta]\right) - \widetilde{f}'_{bl_n}\Big|_{1+\delta} \mathrm{H}_n^{(2)}\left(\Gamma_0[1+\delta]\right)\right)} \, . \tag{25}$$

For the distributed source prescribed by spinning mode (l, q), amplitude $\widetilde{\eta}_n$ is given by

$$\widetilde{\eta}_n(k_z) = \pi^2 \xi_{lq} P_{lq} (-1)^{l+n} \mathrm{e}^{-\mathrm{i}(l-n)\beta} \left(k_0 + k_z M_\infty\right) \Psi_{lq} \mathrm{H}_{l-n}^{(2)}(\Gamma_0 b) \, . \tag{26}$$

Combining these results, on the surface of the cylinder, the pressure can be calculated via

$$\hat{p}_t\left(a_0, \bar{\phi}, \bar{z}\right) = \frac{1}{(2\pi)^2} \sum_{n=-\infty}^{\infty} \left\{ \int_{-\infty}^{\infty} \widetilde{\alpha}_n(k_z)\, \mathrm{e}^{-\mathrm{i}k_z\bar{z}} \mathrm{d}k_z \right\} \mathrm{e}^{-\mathrm{i}n\bar{\phi}} \, . \tag{27}$$

III. Validation

Figure 3 shows the process to calculate $\widetilde{\alpha}_n(k_z)$. Equation (22) is integrated using the Runge–Kutta Ordinary Differential Equation solver *ode45* in Matlab, starting from the surface of the cylinder at $\bar{r} = 1$, up to the edge of the boundary layer $\bar{r} = 1 + \delta$. If, for the prescribed value of k_z, there is a critical layer, the ODE solver integrates to near the critical layer at $\bar{r} = \bar{r}_c - \varepsilon$. Then the Frobenius solution is used to the bridge the layer, and the ODE solver is restarted on the other side of the critical layer at $\bar{r} = \bar{r}_c + \varepsilon$. The integration continues until the edge of the boundary layer at $\bar{r} = 1 + \delta$. At this point the boundary layer solution is matched to the uniform flow amplitude, which determines $\widetilde{\alpha}_n(k_z)$.

Having calculated $\widetilde{\alpha}_n(k_z)$, the total pressure on the surface of the cylinder is given in terms of the complex Fourier series in Equation (27); each amplitude coefficient in this series requires numerical evaluation of an inverse Fourier transform (integral with respect to the axial wavenumber k_z). Determining the convergence of the k_z-integral is straightforward in the absence of the boundary layer and is discussed in McAlpine, Gaffney and Kingan ([6], Sec. IIIC, pp. 1320–1321). McAlpine *et al.* specified finite integration limits, $-K < k_z < K$, which can be determined by the asymptotic expansion of the Hankel function $\mathrm{H}_n^{(2)}$ for large argument ([6], Eq. (51)); outside this range the integrand is exponentially small. It can also be shown that there is no significant contribution to the k_z-integral owing to having to circumvent the branch points at k_z^- and k_z^+. However, in the current work, the inclusion of the boundary-layer means that part of $\widetilde{\alpha}_n(k_z)$ is calculated numerically.

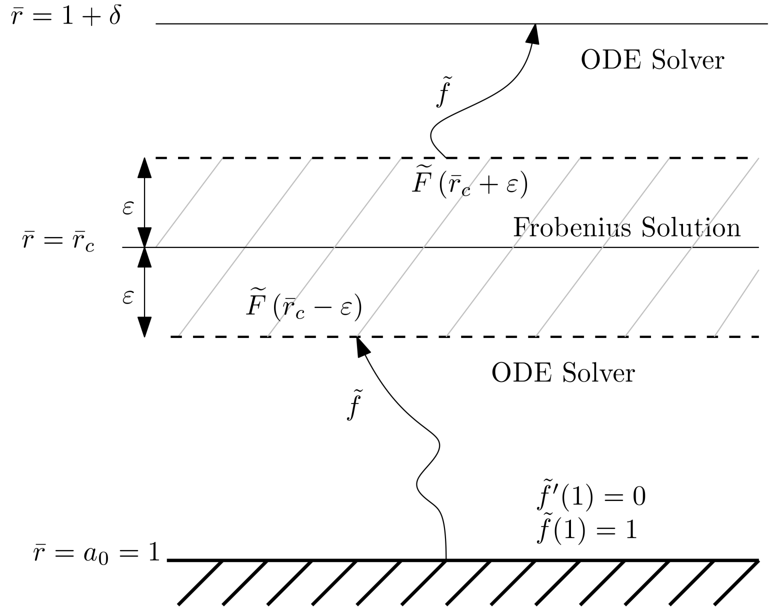

Figure 3: Illustration showing the method to solve the Pridmore-Brown equation in the boundary layer. The numerical solution obtained using a standard ODE solver, for harmonic n, is matched to the Frobenius solution either side of the critical layer, in order to bridge the critical point $\bar{r}_c$.

Owing to this, the limits $\pm K$ are determined numerically for each individual integral. Typically it is found that $\widetilde{\alpha}_n(k_z)$ decays rapidly outside the range $k_z \in (k_z^-, k_z^+)$. Also, as outlined in Table 1, the integral is split into three parts $I_1 + I_2 + I_2$. Each part is evaluated separately using *quadgk* in Matlab which is an adaptive quadrature routine designed for integrating between singularities.

In the following sections, first the accuracy of the numerical integration across the boundary layer is verified, and then it is checked that the method gives the correct result when the boundary-layer thickness $\delta = 0$. The convergence of the Fourier series, and the optimum width of the critical layer where the Frobenius solution is applied is evaluated. Finally, a result from the method is compared against a published result.

A. Code verification

A standard Runge–Kutta numerical integration routine is used to solve the Pridmore-Brown equation in the boundary-layer region. The solver can be checked by comparison with an analytic solution for the special case $M(\bar{r}) = M_\infty$. In this case, the Pridmore-Brown equation (16) reduces to Bessel's differential equation. Hence, the normalised pressure can be expressed in terms of Bessel functions, in the form

$$\widetilde{f_{bl_n}} = A_n J_n(\Gamma_0 \bar{r}) + B_n Y_n(\Gamma_0 \bar{r}) \, . \tag{28}$$

The amplitude coefficients are determined by the boundary conditions.

Having verified the accuracy of the numerical integration solver, the boundary-layer refraction cylinder scattering code has been verified by comparing the numerical results with results obtained using the basic cylinder scattering code. The basic code is for uniform flow only. Verification of this code is published in McAlpine, Gaffney and Kingan [6]. Accordingly, all the verification results have been obtained by setting $M(\bar{r}) = M_\infty$, i.e. a finite thickness boundary-layer region is specified, but in this region, the flow velocity is set equal to the free stream velocity outside the boundary layer. This means that the term involving M' in Equation (22) is zero; otherwise, implementation of the boundary-layer refraction cylinder scattering code is identical to simulations when $M(\bar{r})$ is not set equal to a constant.

Figure 4a shows the normalised total pressure in Sound Pressure Levels on the unfurled cylinder, calculated using the boundary-layer refraction cylinder scattering code. The uniform flow code developed previously was used as the reference result to calculate the relative error shown in Figure 4b,c. The pressure field has been calculated in the axial region from $\bar{z} = 0$ (source plane) up to $\bar{z} = 5$. Numerical results from the two methods show excellent agreement. The relative error is significantly less than 1 % over the whole domain. This result is very similar for different values of δ.

B. Convergence

The critical point, where $k_0 + k_z M(\bar{r}_c) = 0$, will occur at $k_z = -k_0/M(\bar{r}_c)$, which lies in the region $k_z \leq -k_0/M_\infty < k_z^-$. Consequently, the critical layer will only affect integral I_1. The evaluation of I_1 will be affected by altering the width of the critical layer and/or the number of interpolation points used to evaluate $\widetilde{\alpha}_n$.

The inverse Fourier transform integral (27) is computationally expensive, and has to be evaluated at each axial position. However, the function $\widetilde{\alpha}_n(k_z)$ does not depend on $\bar{z}$, therefore $\widetilde{\alpha}_n$ may be pre-calculated for each harmonic order n. A spline interpolation routine is implemented to evaluate $\widetilde{\alpha}_n(k_z)$ at any value of k_z required by the adaptive numerical integration solver.

Since the function $\widetilde{\alpha}_n(k_z)$ can be highly oscillatory, the number of interpolation points must be sufficient to ensure accurate interpolation, and thus accurate evaluation of the inverse Fourier transform. Figure 5 shows the effect of evaluating integral I_1 on taking different widths of the critical layer where the Frobenius solution is used in place of the numerical integration. The frequency used in these results is the same which is used subsequently in Figure 6. In Figure 5(a) it is seen that as the number of interpolation points of $\widetilde{\alpha}_n(k_z)$ is increased, convergence is achieved reasonably quickly. The number of interpolation points, N, has been scaled by dividing by $k_z^\Delta = k_z^+ - k_z^-$.

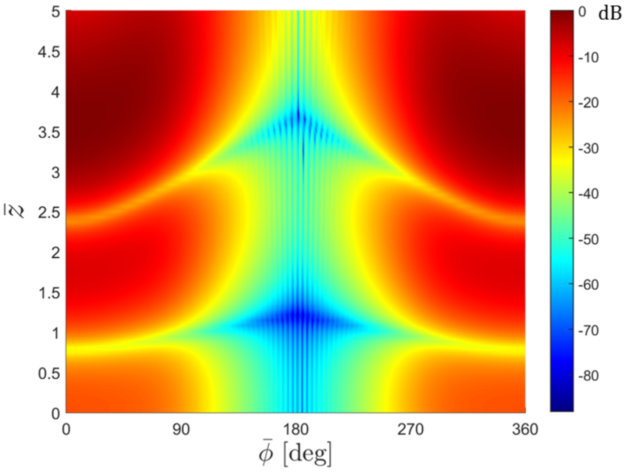

(a)

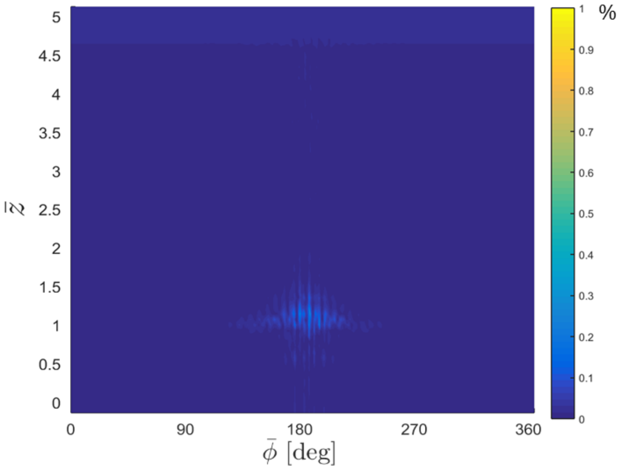

(b)

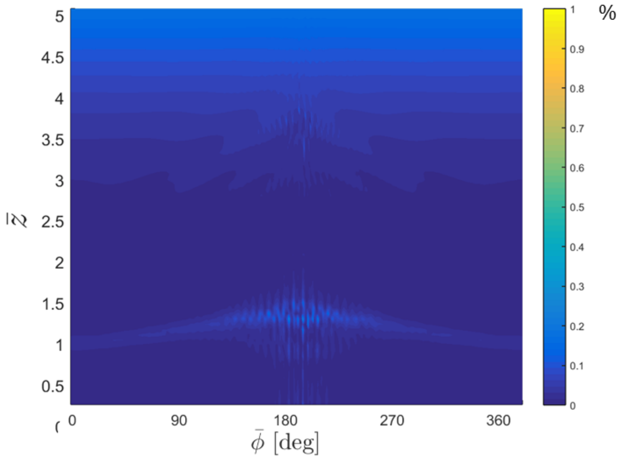

(c)

Figure 4: Comparison of the boundary-layer refraction and uniform flow cylinder scattering codes: (a) SPL; (b) relative error, $\delta = 0.01$; (c) relative error, $\delta = 0.1$. The relevant parameters in this example are $(l, q) = (16, 1)$, $k_0 a = 20$, $a = 0.6$, $b = 6$ and $M_\infty = 0.7$.

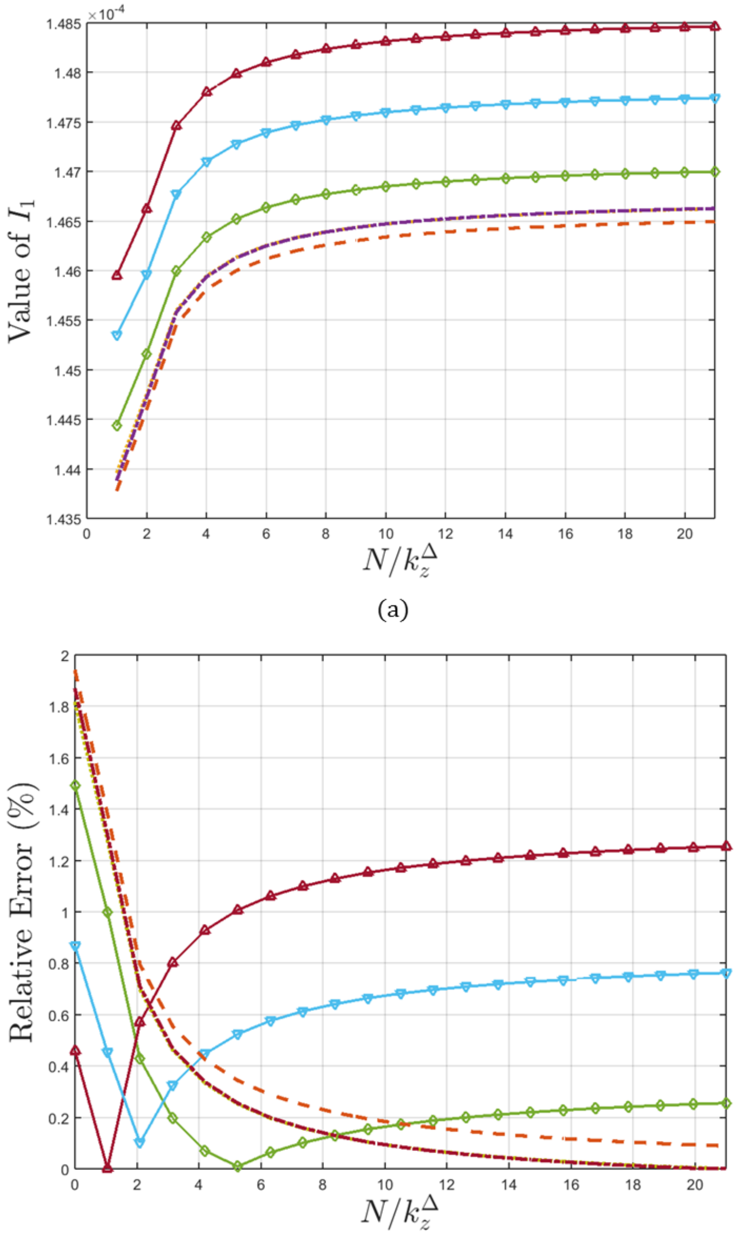

(a)

(b)

Figure 5: Effect of width of the critical layer (Frobenius solution) and number of interpolation points used to evaluate I_1: (a) absolute error; (b) relative error. The relevant parameters in this example are $(l, q) = (0, 1)$, $k_0a = 0.0524$, $a = 0.01$, $b = 1.5$, $\delta = 0.125$ and $M_\infty = 0.7$. Key: ε = 0.0002 (orange dashes), 0.001 (yellow dots), 0.002 (purple dash dots), 0.003 (green $\diamond$), 0.005 (cyan ∇) and 0.01 (maroon $\triangle$).

The Frobenius series has been truncated at $\mathrm{O}(\varsigma^3)$. Although it is required that the width of the critical layer is small, if ε is too small the ODE solver will lose accuracy. To establish an appropriate value for ε, the width of the Frobenius solution was varied whilst calculating the value of the integral I_1 for the zeroth Fourier harmonic. In Figure 5(b) it is seen that, at this relatively low frequency, the width of the critical layer has little effect on the value of I_1. The results for $\varepsilon = 0.001$ and 0.002 are almost exactly the same.

In summary, these convergence results show that the ideal width of the critical layer, where the Frobenius series solution is applied, is between $\varepsilon = 0.002$ and 0.003. The reference value selected was $\varepsilon = 0.0025$. Also these results show that the integral converges with the number of points $N \approx 10\, k_z^{\Delta}$. This reference value was selected for all the results.

C. Comparison with Lu [4]

Lu [4] examined the problem of a point monopole source located adjacent to a rigid cylinder, and calculated the pressure on the cylinder including the effect of boundary-layer refraction. In Ref. [4], Fig. 6, Lu plotted predictions of the difference between the SPL on the cylindrical fuselage at $\bar{\phi} = 0$ and the corresponding value of the SPL in the free field (in the absence of the cylinder). Negative values indicate shielding. We have sought to use this example to provide another benchmark case for our boundary-layer refraction cylinder scattering code. In order to compare the results, the radius, a, of the disc source is set to be much less than the acoustic wavelength of the plane wave mode. This means that the disc source should closely approximate a monopole, and the results can be compared against the result shown in Lu [4].

The comparison is shown here in Figure 6. The two predictions show similar agreement downstream of the source. However, upstream of the source, the two predictions do not compare well.

Slightly upstream of the source, the prediction by Lu has an extremely rapid roll off, indicating extremely high shielding upstream. The prediction for the compact disc source has a lesser roll off rate, indicating less shielding. However, the shielding is still substantial with increasing axial distance upstream of the source. It is not clear why in Lu's prediction, the shielding is a maximum at $\bar{z} \approx 0.75$, but then the shielding reduces further upstream. It is difficult to draw a definitive conclusion from this result because there is only one example to compare against.

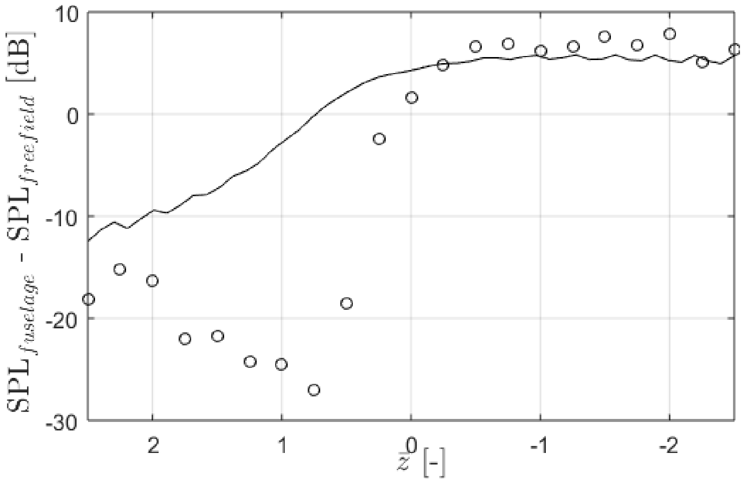

Figure 6: Difference in the predicted SPL between the installed fuselage pressure and the incident field pressure at $\bar{\phi} = 0$. The relevant parameters are $(l, q) = (0, 1)$, $k_0 a = 0.0523$, $a = 0.01$, $b = 1.5$, $\delta = 0.125$ and $M_\infty = 0.7$. Key: Boundary-layer refraction cylinder scattering code (solid line) and prediction by Lu [4] (circles).

IV. Illustrative results

Illustrative results are shown of predictions of the sound pressure levels on a cylindrical fuselage. The results illustrate how the levels are affected by changes in the source characteristics and changes in the flow characteristics. All the predictions show the levels on the cylinder in the axial range

$0 < \bar{z} < 5$, which roughly is comparable with the length of the fuselage forward of the engine, for airplanes with wing-mounted engines. For clarity, the results are shown for one source, on the right hand side of the fuselage, and for a single mode. Results are compared for a thin boundary-layer, $\delta = 0.01$, or a relatively thick boundary-layer, $\delta = 0.1$.

Published values for the typical boundary-layer thickness on an aircraft fuselage are difficult to find. Recently some realistic predictions were in Ref.[14]. In this paper the maximum thickness $(99\% M_\infty)$ is around $0.1a_0$ in the plane of the engines. Flat plate predictions for a turbulent boundary layer thickness also predict a value for δ of around $0.1a_0$ at this plane.

Two metrics are used to evaluate the effect of the boundary layer on the levels on the cylinder. First, we examine the difference in the predicted SPL on the cylinder with and without the boundary layer, i.e.

$$\Delta\,[\mathrm{dB}] = \mathrm{SPL}_{bl} - \mathrm{SPL}. \tag{29}$$

The difference Δ is useful for predicting the reduction in the 'hot spot' (region where the SPL on the cylinder is at a maximum). However, just examining the Δ's can be misleading. For example, a large Δ predicted on the far side of the cylinder will not be significant because it has been observed that with uniform flow, i.e. no boundary-layer shielding, the levels on the far side of the cylinder are low. A large reduction in these levels is not important to cabin noise.

Next, to obtain a more overall view of the boundary-layer effect we introduce a simple 'shielding' coefficient, denoted by S. The shielding coefficient is defined as the ratio of the area-averaged mean square pressure over the cylinder's surface, with and without the boundary layer included in the prediction model. This value is, in turn, roughly proportional to the amount of the acoustic energy of the incident wave refracted away from the cylinder by the boundary layer. Accordingly, we define

S by

$$S = \frac{(1/A)\int_A \overline{p^2}_{bl}\,\mathrm{d}A}{(1/A)\int_A \overline{p^2}\,\mathrm{d}A} \approx \frac{\sum^M \overline{p^2}_{bl}}{\sum^M \overline{p^2}}, \tag{30}$$

where in practice it is sufficient to evaluate S via a sum of the predicted mean square pressures over the M grid points distributed over the cylinder's surface. The value of S will be between 0 and 1, where zero represents total shielding and unity represents no shielding.

The results shown in Sections A.,B. examine predictions of S for three different boundary-layer profiles. These profiles are *linear* (δ_l), *quarter-sine* (δ_s) and a representative 'turbulent' *seventh-power-law* mean-flow profile (δ_t), where for each profile δ denotes the boundary-layer thickness. A quarter-sine velocity profile was chosen for the source parametric study in Sec. A.. This profile is reasonably similar to a Pohlausen profile which was used by Lu [4]. In Sec. B. predictions for the different boundary-layer profiles are compared. For reference, all the relevant profiles are plotted in Figure 7. For each profile, the location of the critical point can be found exactly. This location must be calculated numerically for more complicated profile shapes.

A. Source characteristics

In this section the source characteristics are changed whilst the boundary-layer flow profile and free-stream velocity are kept fixed. However, the effect of a thin or thick boundary-layer, having the same profile shape, is investigated.

Figure 8(a–c) show examples of the results. Figure 8(a) shows the result with uniform flow, $\delta = 0.0$. This case is used as a reference to compare with a thin boundary-layer $\delta = 0.01$ shown in Figure 8(b), and a thick boundary-layer $\delta = 0.1$ shown in Figure 8(c). Note that all results are normalised, so that the maximum SPL is equal to zero with uniform flow.

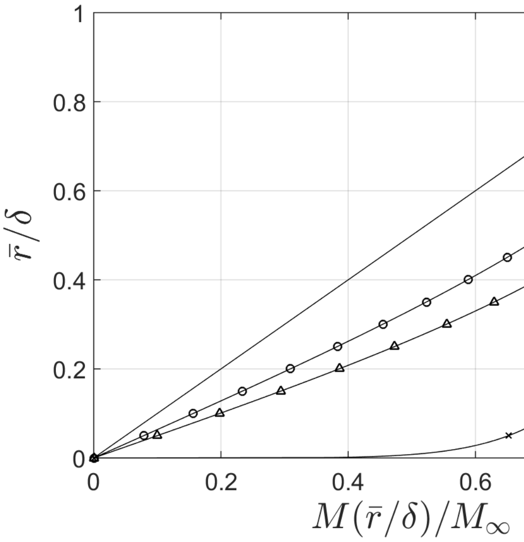

Figure 7: Normalised boundary-layer profiles. Key: linear (solid line), $1/7$th-power law (×), quarter sine (○) and Polhausen (△).

The value of the source Helmholtz number k_0a will determine the structure of the source's polar directivity pattern. For the plane wave mode, at very low values of k_0a, in this limit the source becomes omnidirectional. For non-plane-wave modes, the level at the intake duct's axis will be zero. But whilst the frequency remains low, no side lobes are present. As the frequency increases, along with the principal lobe of radiation, more and more side lobes will be present. For a state-of-the-art turbofan engine, a typical k_0a value of the blade passing frequency tone is around 20. In the examples in this section, the source Helmholtz numbers are taken to be $k_0a = 5$, 10 and 20.

Figure 9 plots the value of Δ at $\bar{\phi} = 0$ for the three different source Helmholtz numbers. It is seen that for increasing frequency (k_0a) the refraction effect of the boundary layer increases. In the plane of the source the shielding is a moderate 2-3 dB for a thin boundary-layer profile, however the shielding for a thick profile is 10 dB for the high frequency case. At high frequencies, refraction by the boundary layer can be more significant since the acoustic wavelength will be comparable or smaller compared to the boundary-layer thickness.

Further upstream of the source plane, the shielding increases. More shielding is expected upstream because the angle of incidence relative to the boundary layer decreases. Even for the lowest value of $k_0 a$ for a thin boundary layer, at $\bar{z} = 5$, the value of Δ is around 18 dB. At shallow angles, the wave will be highly refracted by the shear layer. In general, shielding increases with both increasing frequency and boundary-layer thickness; also shielding increases as the grazing angle relative to the boundary layer becomes less.

For $k_0 a = 5$, the polar directivity of the source has only one lobe. For the other cases, side lobes are present. The locations of nulls in the source's polar directivity are slightly shifted by the boundary-layer; the effect of this can be seen in the levels on the surface of the cylinder, via dips in the plots of Δ.

The 'shielding' coefficient S calculated for the three different source Helmholtz numbers are shown on Figure 9 next to the relevant line. At frequency $k_0 a = 5$, and for a thin boundary-layer, $S = 0.37$. In this case the area-averaged mean square pressure with the boundary layer is 63 % less than without the boundary layer included in the modelling. As a rough approximation, around two-thirds of the incident energy is refracted away from the cylinder's surface by the boundary layer. With a thick boundary layer the reduction is close to 95 % ($S = 0.056$). As is seen in Figure 9, large reductions are present on the near side of the cylinder adjacent to the source. On the cylinder's surface at $\bar{r} = a_0$, the shear for the quarter-sine profile is strongest. Thus as the waves creep around the cylinder, the wave is immersed in the boundary layer, and strong shielding occurs on the far side as well.

Figure 10 shows the normalised SPL on the surface of the cylinder for mode $(l, q) = (24, 1)$. The frequency $k_0 a = 20$ which means that this mode is only just cut on. The source directivity is such

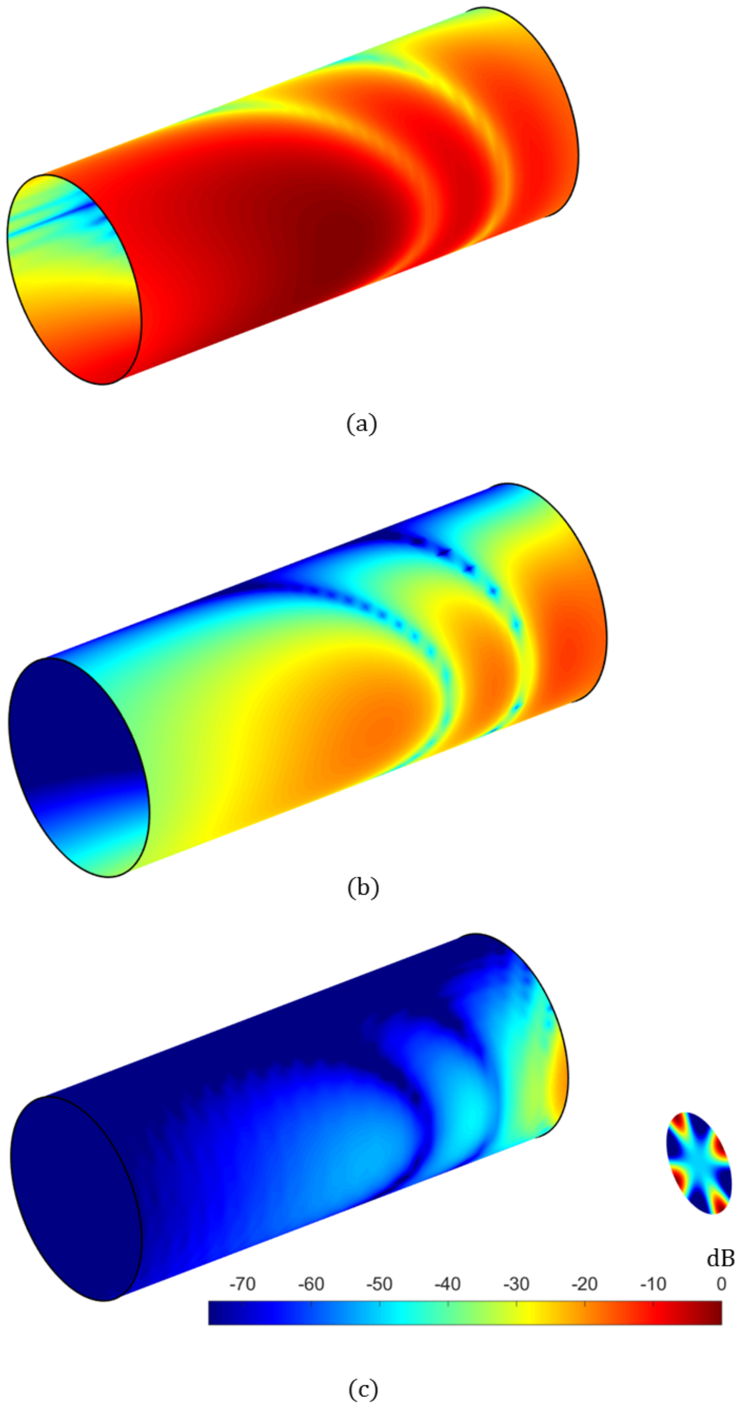

Figure 8: Normalised total SPL on the surface of the cylinder: (a) uniform flow, $\delta = 0.0$; (b) $\delta = 0.01$; and, (c) $\delta = 0.1$. The source is included in (c) for perspective. The relevant parameters are $(l, q) = (4, 1)$, $k_0 a = 10$, $b = 3$ and $M_\infty = 0.75$.

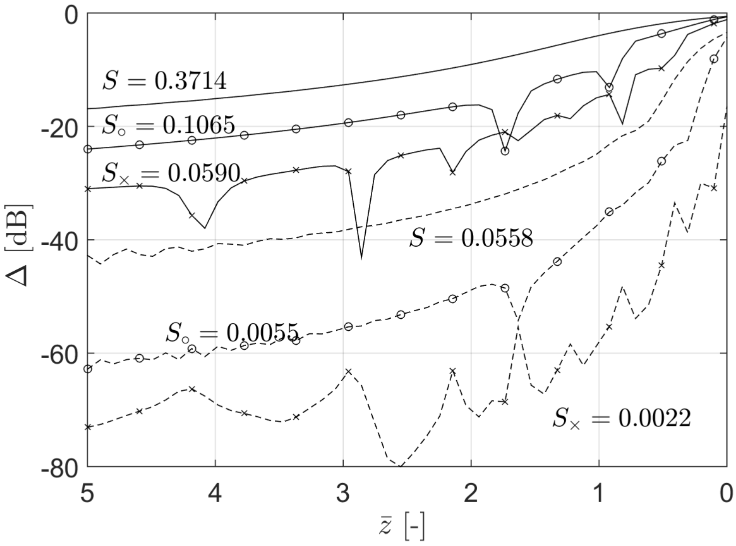

Figure 9: Prediction of Δ at $\bar{\phi} = 0$ for different values of the source Helmholtz number k_0a. The relevant parameters are $(l, q) = (4, 1)$, $a = 0.5$, $b = 3$ and $M_\infty = 0.75$. Key: Solid lines denote a boundary layer of thickness $\delta = 0.01$ and dashed lines are for $\delta = 0.1$. The varying Helmholtz numbers are $k_0a = 5$ (no symbol), $k_0a = 10$ $(\circ)$, and $k_0a = 20$ $(\times)$.

δ	$ka = 10$	$ka = 20$	
	l	l	
	4	4	24
0.01	0.1065	0.0590	0.2713
0.1	0.0055	0.0022	0.0119

Table 2: ‘Shielding’ coefficient S for the examples shown in Figures 8 and 10. In Figure 8, the frequency $k_0a = 10$ and the mode $(l, q) = (4, 1)$. Note that the mode $(l, q) = (24, 1)$ is cut-off at this frequency. In Figure 10, the frequency $k_0a = 20$ with the mode $(l, q) = (24, 1)$. For comparison, also the values of S for mode $(l, q) = (4, 1)$ which are shown at this higher frequency.

that only a single lobe intersects with the cylinder at an axial position close to the source plane. On the near side of the cylinder, there is some increase in the shielding as the boundary-layer thickness is increased, but the overall effect is less comparing Figure 10 with the previous example shown in Figure 8. This is due to the angle of incidence of the mode; for a mode that is only just cut on, the angle will be close to 90° relative to the boundary layer. A wave impinging at a shallower angle is far more susceptible to the effects of the boundary layer. The values of the ‘shielding’ coefficient S calculated for the examples shown in Figures 8 and 10 are shown in Table 2.

An alternative way to look at the effect of the boundary layer can be demonstrated by plotting an example of the function $\widetilde{\alpha}_n(k_z)$, with and without the boundary layer, as shown in Figure 11. The function $\widetilde{\alpha}_n$ is largely unchanged for negative axial wavenumbers (waves travelling in the same direction as the flow), but the large fluctuations for positive axial wavenumbers are significantly reduced when the boundary layer is included in the calculation. In the Fourier domain the boundary

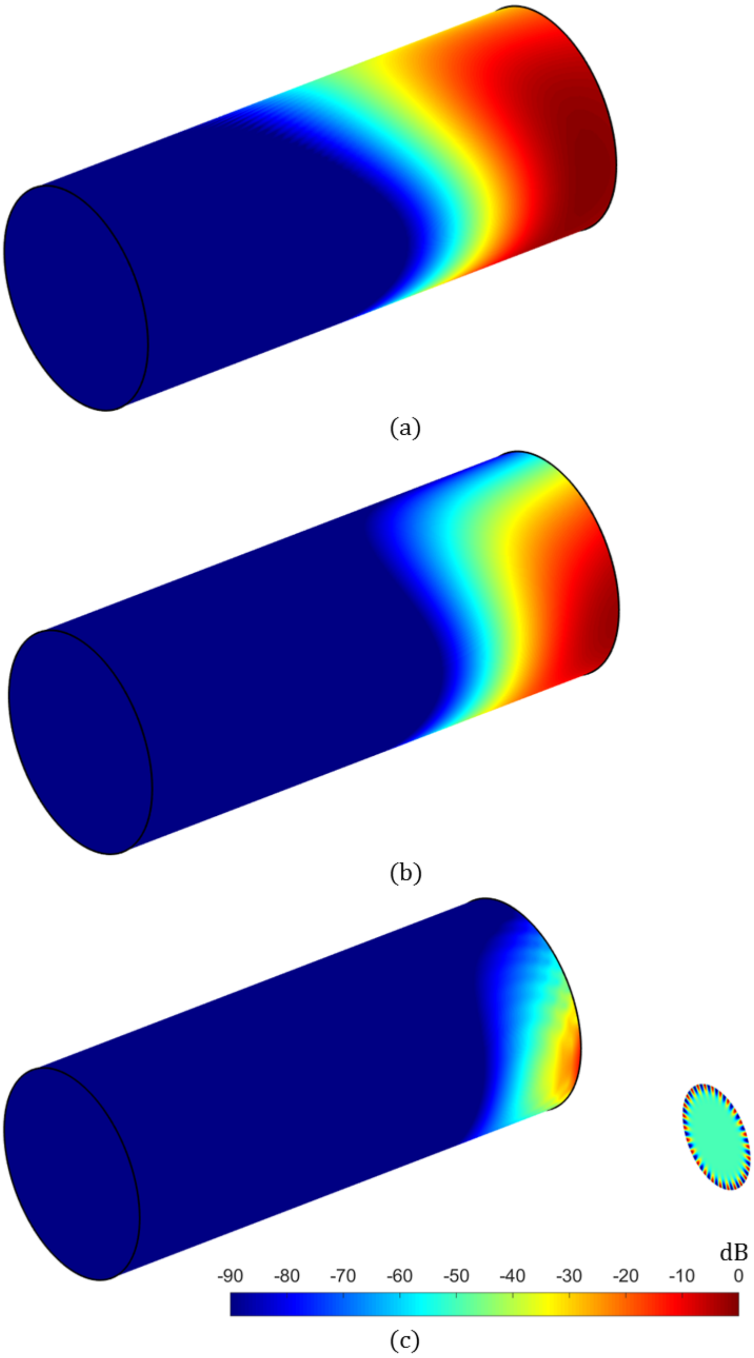

Figure 10: Normalised total SPL on the surface of the cylinder: (a) uniform flow, $\delta = 0.0$; (b) $\delta = 0.01$; and, (c) $\delta = 0.1$. The relevant parameters are $(l, q) = (24, 1)$, $k_0 a = 20$, $a = 0.5$, $b = 3$ and $M_\infty = 0.75$

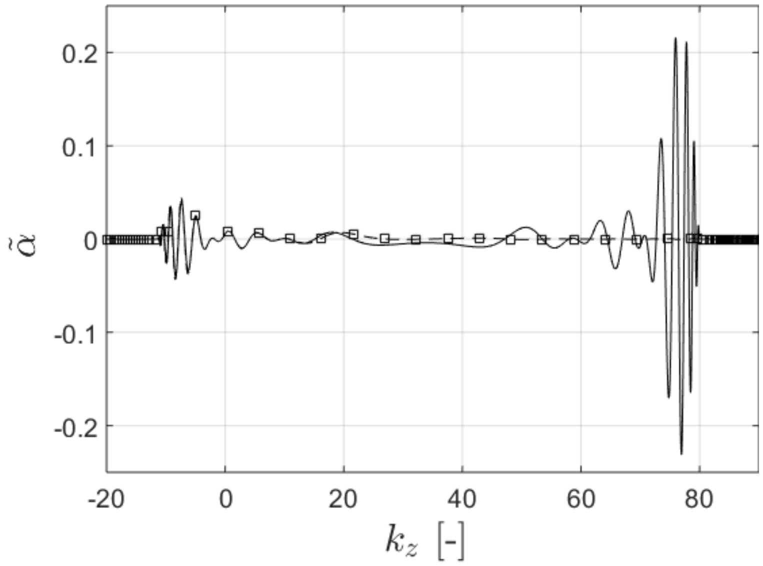

Figure 11: The function $\widetilde{\alpha}_n$ for the zeroth azimuthal mode. The relevant parameters are $k_0 a = 10$, $a = 0.5$, $b = 3$ and $M_\infty = 0.75$. Key: $\delta = 0$ (solid line); $\delta = 0.1$ (dashed line and squares).

layer acts as a low-pass filter.

We note that although the polar directivity of the spinning mode source is axisymmetric, on the rigid cylinder the pressure patterns are slightly asymmetric. It can be shown that

$$p_t\left(l, -\bar{\phi}\right) = (-1)^l\, p_t\left(-l, \bar{\phi}\right). \tag{31}$$

Note the phase change for odd azimuthal orders.

B. Flow characteristics

In this section the flow characteristics are changed whilst the source is kept fixed. The source frequency is $k_0 a = 20$ and source mode is $(l, q) = (16, 1)$. Results are compared for the linear, quarter-sine and $1/7$th power law turbulent mean-flow boundary-layer profiles, as shown in Figure 7. The effect of varying the flow speed can be found in Gaffney, McAlpine and Kingan [15]

Figure 12(a) shows a plot of the values of Δ at $\bar{\phi} = 0$ for the three different boundary-layer

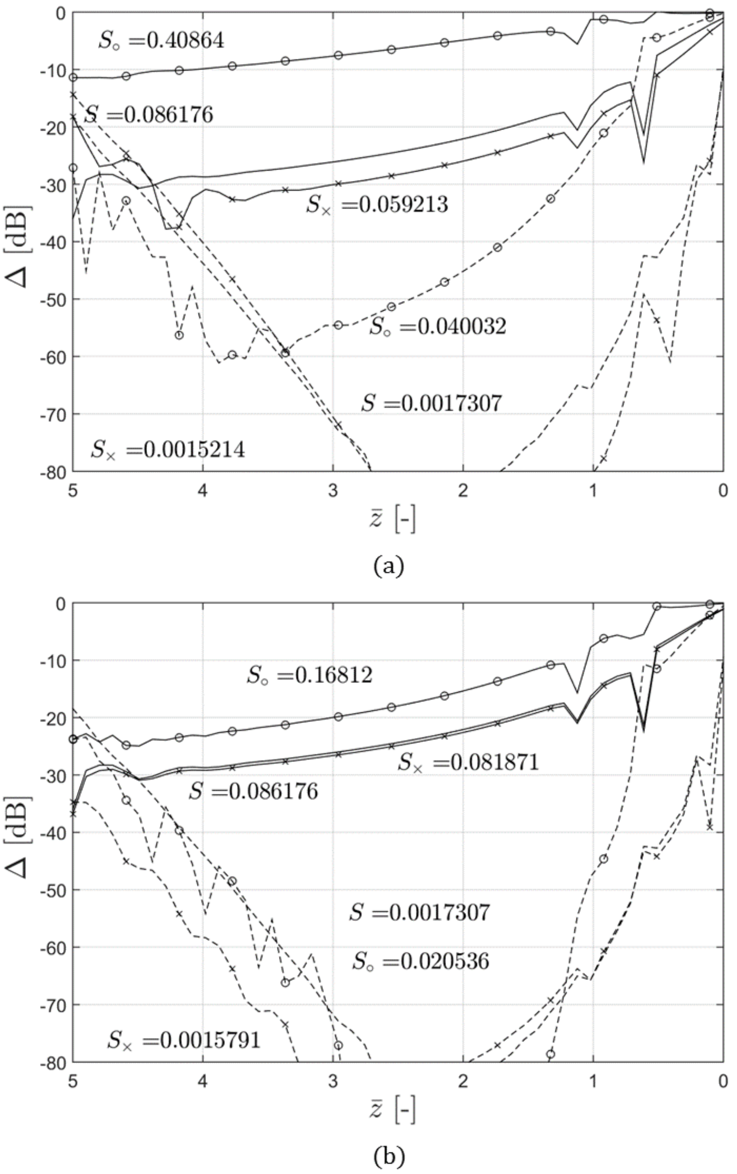

(a)

(b)

Figure 12: Prediction of Δ at $\bar{\phi} = 0$ for two different boundary-layer profiles: (a) δ fixed; (b) $\delta^\star$ fixed. The relevant parameters are $(l, q) = (16, 1)$, $k_0 a = 20$, $a = 0.5$, $b = 3$ and $M_\infty = 0.75$. Key: thin boundary-layer (solid lines) or thick boundary-layer (dashed lines); boundary-layer profiles, linear $(\times)$, quarter-sine (no symbol), 1/7th-power law $(\circ)$.

profiles. Results are shown for both the thin and thick boundary-layers. The shielding predicted for the linear and quarter-sine boundary-layer profiles are fairly similar. For this example, the mode is moderately cut-on, so moving further upstream, at $\bar{z} = 5$ the levels on the cylinder are very low with or without the boundary layer included in the prediction scheme.

The power law mean-flow profile is predicted to cause significantly less shielding along the cylinder. The 'shielding' coefficient is much larger compared with the other profiles, which corresponds to relatively higher pressure amplitudes on the cylinder's surface.

The results in Figure 12(b) are for the same profiles as in (a), however the thickness of the boundary layer profiles have been modified so that the displacement thicknesses $\delta^\star$ of each profiles are identical. It is seen that, in this case, the shielding is very similar. Predictions for the linear and quarter-sine profiles are almost identical. Also, the difference between the power-law profile and the linear profile has reduced from 15 dB at $\bar{z} = 3$ to around only 3 dB, for predictions with the profiles having the same value of $\delta^\star$. These results suggest that the size of the displacement thickess is a more important factor vis-á-vis the boundary-layer profile shape.

V. Conclusions

A theoretical method has been developed which can be used to predict the acoustic pressure on a cylindrical fuselage due to a disc source located adjacent to the cylinder, including the effect of refraction by the fuselage boundary layer. The key new aspect of this work is the use of a disc source to represent sound radiation from a spinning mode exiting a cylindrical duct. Previous similar analysis of cylindrical fuselage boundary-layer refraction effects have employed a point source [4] or a propeller/open rotor source [2, 3, 12, 5]. The application of the current work is the prediction of the radiated pressure field on an aircraft's fuselage, which is relevant for the assessment of cabin noise, from an installed turbofan aero-engine. This method can be used for single-mode calculations of the pressure on a cylindrical fuselage, with arbitrary boundary-layer profile and thickness. The model is a simple representation of a fan tone radiated from a turbofan intake duct. The methodology extends the solution given by McAlpine, Gaffney and Kingan [6] which omitted the fuselage boundary layer, and assumed uniform flow everywhere. Illustrative results have shown that the sound pressure levels on the surface of the cylinder, upstream of the source, are predicted to be greatly reduced for simulations which include the fuselage boundary layer, even for a thin boundary layer. The boundary-layer 'shielding' is seen to be most effective for well cut on modes. This is because the incident pressure grazes the boundary layer, and is more susceptible to refraction.

In order to quantify the effect of the boundary layer, a ratio termed the 'shielding' coefficient has been introduced. This coefficient provides a measure of the total shielding, over the whole area of the cylinder. It is seen that with a thick boundary-layer profile, most of the acoustic energy will be shielded, and since the sound energy is refracted away from the cylinder's surface, the levels on the cylindrical fuselage are predicted to be low compared to the levels which are predicted based on a uniform free-stream velocity.

Future work will focus on replacing the disc source which is used to model a spinning mode exiting a cylindrical duct by a more sophisticated technique, employing the Wiener–Hopf solution to model sound radiation from a turbofan intake. This method will include diffraction and scattering effects caused by the duct termination, which have been omitted in the current method. Thus, as well as providing a more realistic model of sound radiated from an intake duct, also the refractive effects of the fuselage boundary layer will be examined, both upstream and downstream of the source.

All data supporting this study are openly available from the University of Southampton repository at http://dx.doi.org/10.5258/SOTON/400423

Acknowledgments

The authors wish to acknowledge the continuing financial support provided by Rolls-Royce plc through the University Technology Centre in Gas Turbine Noise at the Institute of Sound and Vibration Research. The first author also acknowledges the financial contribution from the EPSRC via the University of Southampton's DTP grant.

References

[1] J. Bowman, T. Senior, and P. Uslenghi, eds., *Electromagnetic and Acoustic Scattering by Simple Shapes* (Horth-Holland Publishing Co., Amsterdam) (1969).

[2] D. Hanson, “Shielding of prop-fan cabin noise by the fuselage boundary layer”, Journal of Sound and Vibration **22**, 63–70 (1984).

[3] D. Hanson and B. Magliozzi, “Propagation of propeller tone noise through a fuselage boundary layer”, Journal of Aircraft **22**, 63–70 (1985).

[4] H. Lu, “Fuselage boundary-layer effects on sound propagation and scattering”, American Institute of Aeronautics and Astronautics Journal **28**, 1180–1186 (1990).

[5] H. Brouwer, “The scattering of open rotor tones by a cylindrical fuselage and its boundary layer”, Proceedings of the 22nd AIAA/CEAS Aeroacoustics conference, Lyon, France, AIAA paper no. 2016-2741 16 pp. (30 May–1 June, 2016).

[6] A. McAlpine, J. Gaffney, and M. Kingan, “Near-field sound radiation of fan tones from an installed turbofan aero-engine”, Journal of the Acoustical Society of America **138**, 131–1324 (2015).

[7] J. Tyler and T. Sofrin, “Axial flow compressor noise studies”, SAE Transactions **70**, 309–332 (1962).

[8] S. Hocter, “Exact and approximate directivity patterns of the sound radiated from a cylindrical duct”, Journal of Sound and Vibration **227**, 397–407 (1999).

[9] E. Rice, M. Heidmann, and T. Sofrin, “Modal propagation angles in a cylindrical duct with flow and their relation to sound radiation”, 17th Aerospace Sciences Meeting, New Orleans, LA, AIAA paper no. 79-0183 (15–17 January, 1979).

[10] E. Brambley, M. Darau, and S. Rienstra, “The critical layer in linear-shear boundary layers over acoustic linings”, Journal of Fluid Mechanics **710**, 545–568 (2012).

[11] In fact this is the opposite branch to that selected in Ref. [3], because in this current work the time-dependence is $\exp\{\mathrm{i}\omega t\}$, whereas in Ref.[3] the authors used $\exp\{-\mathrm{i}\omega t\}$.

[12] I. Belyaev, “The effect of an aircraft’s boundary layer on propeller noise”, Acoustical Physics **58**, 425–433 (2012).

[13] This assumes that the boundary-layer mean flow profile does not allow solutions of the Pridmore-Brown equation which are exponentially small at $\bar{r} = 1$.

[14] A. Klabes, C. Appel, M. Herr, and M. Bouhaj, “Fuselage excitation during cruise flight conditions: measurement and prediction of pressure point spectra”, Proceedings of the 21st AIAA/CEAS Aeroacoustics conference, Dallas, TX, AIAA paper no. 2015-3115 23 pp. (22–26 June, 2015).

[15] J. Gaffney, A. McAlpine, and M. Kingan, “Sound radiation of fan tones from an installed turbofan aero-engine: fuselage boundary-layer refraction effects”, Proceedings of the 22nd AIAA/CEAS Aeroacoustics conference, Lyon, France, AIAA paper no. 2016-2878 23 pp. (30 May–1 June, 2016).

List of Figures